Atmos. Chem. Phys., 26, 11473–11489, 2026
https://doi.org/10.5194/acp-26-11473-2026

Atmospheric Chemistry and Physics
Open Access
EGU

Research article

High frequency of urban new particle formation on the Tibetan Plateau: quantifying formation rates, growth rates, and CCN production

Qiqi Mo[1], Longjie Wen[1,2], Gang Zhao[1,3], Chunxiang Ye[4], Jie Sun[1], Weili Lin[1,5], Fengjun Shen[1], Tong Liu[1], Yicheng Gao[1], Yi Chen[4], Tiantian Zhang[1], and Tong Zhu[4]

[1]Key Laboratory of Ecology and Environment in Minority Areas, Minzu University of China, National Ethnic Affairs Commission, Beijing, 100081, China
[2]School of Ecology and Environment, College of Intelligence, Harbin Institute of Technology (Shenzhen), Shenzhen, 518055, China
[3]Key Laboratory of Biodiversity and Environment on the Qinghai-Tibet Plateau, Ministry of Education, Xizang University, Lhasa, 850000, China
[4]SKL-ESPC & SEPKL-AERM, College of Environmental Sciences and Engineering, Institute of Tibetan Plateau, and Center for Environment and Health, Peking University, Beijing, China
[5]Institute of National Security, Minzu University of China, Beijing, 100081, China

Correspondence: Gang Zhao (gangz@muc.edu.cn) and Chunxiang Ye (c.ye@pku.edu.cn)

Received: 24 March 2026 – Discussion started: 29 April 2026
Revised: 12 August 2026 – Accepted: 12 August 2026 – Published: 14 August 2026

Abstract. New particle formation (NPF) strongly influences aerosol number size distributions and cloud condensation nuclei (CCN), yet its characteristics and climatic relevance in high-altitude urban environments over the Tibetan Plateau (TP) remain poorly constrained. We conducted in situ observations at Tibet University (TU) in Lhasa during the spring and autumn observation periods. NPF event frequencies were 86.2 % during the autumn observation period and 62.1 % during the spring observation period. Observation days were classified as NPF, Undefined, or Non-Event days based on PNSD evolution, supported by size-segregated particle number concentrations and particle growth rates. Observation-period comparisons indicate clear differences in the factors associated with NPF: NPF during the autumn observation period may have been favored by greater sulfur-precursor availability, whereas no single dominant controlling factor could be identified during the spring observation period. Estimated CCN concentrations were higher on NPF days (mean ± standard deviation: $(2.3 \pm 1.5) \times 10^3$ cm^{-3}; median: 1.9×10^3 cm^{-3}). Corresponding mean ± standard deviation and median values were $(0.9 \pm 0.4) \times 10^3$ and 0.81×10^3 cm^{-3} on Undefined days and $(1.3 \pm 0.7) \times 10^3$ and 1.1×10^3 cm^{-3} on Non-Event days, respectively. The impact of NPF on CCN depends not only on nucleation, but also on the continued growth and survival of newly formed particles. This study provides new insights into urban NPF characteristics and its potential contribution to CCN on the TP, improving our understanding of aerosol–climate interactions in high-altitude urban environments.

Published by Copernicus Publications on behalf of the European Geosciences Union.

1 Introduction

The Sixth Assessment Report of the Intergovernmental Panel on Climate Change (IPCC) highlights that the aerosol climatic effect is a major source of uncertainty in climate change assessment, primarily attributed to the spatio-temporal variability of aerosol concentration and size distribution (Arias et al., 2021). New Particle Formation (NPF) and subsequent particle growth significantly alter aerosol concentration, size distribution, and Cloud Condensation Nuclei (CCN) concentration (Hong et al., 2023). Endowed with unique geographical and atmospheric conditions, the Tibetan Plateau (TP) hosts aerosols that are prone to long-distance transport. This capability allows TP aerosols to modify atmospheric concentration and cloud properties along their path more readily than those in low-altitude regions, thereby impacting both regional atmospheric environment and global climate (Hu et al., 2024). Thus, in-depth exploration of NPF patterns over the TP is crucial for accurately evaluating TP aerosol impact on the global atmosphere and climate.

NPF has also been frequently observed at high-altitude mountain and free-tropospheric sites outside the TP, where mountain-valley circulation, boundary-layer transport, and low-temperature conditions can strongly influence precursor supply and particle formation. At the Nepal Climate Observatory–Pyramid in the Himalayas, frequent NPF was previously observed under the influence of valley winds (Venzac et al., 2008). More recent molecular-level observations at the same site showed that up-valley transport supplied gaseous precursors that were oxidized into low-volatility organic compounds, producing new biogenic particles that could subsequently enter the free troposphere (Bianchi et al., 2021). At the Chacaltaya high-altitude station in Bolivia, NPF and subsequent particle growth produced substantial enhancements in CCN-relevant particle concentrations under both boundary-layer-influenced and free-tropospheric conditions (Rose et al., 2017). These studies demonstrate that high-altitude NPF can be strongly affected by vertical transport and organic precursor chemistry. In contrast, Lhasa represents a high-altitude urban environment influenced by traffic, combustion, construction activities, and elevated anthropogenic gaseous precursors. It therefore provides an opportunity to investigate how urban emissions modify mountain NPF processes that have previously been studied mainly at remote background sites.

Research on NPF in the TP background atmosphere is extensive, leading to a comprehensive understanding of its environmental and climatic effects. For instance, a study at the National Atmospheric Background Monitoring Sub-station on Moshi Daban Mountain (3295 m a.s.l.) in Menyuan, Qinghai Province (Gao et al., 2025), found that NPF events occurred on approximately 80 % of the observation days. These events typically started in the morning, with aerosol particle sizes rapidly growing from approximately 5 to 150 nm, exhibiting the characteristic "banana-shape" curve. Intensive measurements at Nam Co station (4730 m a.s.l.) in the central TP (Tang et al., 2023) explored NPF frequency and mechanisms, revealing significant seasonal differences: approximately 15 % in the pre-monsoon season but up to 80 % during the summer monsoon. Comprehensive analysis of the CS, gaseous precursors, and meteorological factors, combined with SO_2 and Volatile Organic Compounds (VOCs) simulations, concluded that organics-involved condensation is the dominant NPF mechanism, with CS and gaseous sulfuric acid having negligible influence. Furthermore, the high NPF frequency during the summer monsoon season may be closely linked to frequent southerly and south-westerly airflow. Focusing on the south-eastern TP (Lai et al., 2024), research investigated NPF jointly driven by anthropogenic and biogenic factors. Using field measurements and a chemical transport model, they found frequent NPF events on clear-sky days during the pre-monsoon season, contributing significantly to CCN concentration. Observations confirmed that Highly Oxygenated Organic Molecules (HOM_s) from monoterpene oxidation participate in the nucleation process in this region. Liu et al. (2024) further showed that the frequent NPF at high-altitude sites in the south-eastern TP is mainly driven by HOMs, including products from monoterpene, and unexpectedly, sesquiterpenes and diterpenes oxidation. Moreover, anthropogenic NO_x emissions were found to play a crucial regulatory role in particle nucleation. Overall, NPF frequency is high in the TP background atmosphere, and its formation is closely related to temperature, relative humidity, and chemical precursor concentrations.

Aerosols generated by NPF in the TP background atmosphere can contribute up to half of the total atmospheric aerosol number concentration and significantly enhance CCN concentration. A study at the world's highest station, Chacaltaya (Rose et al., 2017), analysed 61 % of NPF events, finding they led to increased CCN number concentration, with the probability reaching 79 % during the wet season due to faster particle growth. The NPF impact on CCN concentration varies seasonally, causing CCN to increase by a factor of 1.54 and 1.36 in spring and winter, respectively. During the summer monsoon season, at a supersaturation of 1.2 %, aerosol number concentration and CCN concentration surged by a factor of 2 and 0.6, respectively, compared to the pre-monsoon season. Furthermore, considering that small particles formed during NPF may continue to grow to CCN activation size over several days, the potential CCN number during the monsoon season may far exceed instantaneous local measurements (Tang et al., 2023). Comparative observations by Shang et al. (2022) indicated that the NPF contribution to total aerosol and CCN concentrations is more significant in the clean atmosphere than that of the polluted atmosphere.

Despite the extensive work summarized above, our understanding of new-particle formation over the TP remains strongly biased toward remote background sites. The urban TP atmosphere – characterised by markedly stronger primary

emissions and elevated concentrations of both SO_2 and NO_x – has, so far, received no systematic exploration of its NPF characteristics, governing mechanisms, or quantitative contribution to CCN. This knowledge gap hampers the accurate representation of aerosol sources in regional climate models and precludes a full assessment of the role of urban NPF over the TP in continental CCN budgets. To fill this gap, we carried out seasonal-scale particle number size distribution (PNSD) measurements in Lhasa (3650 m a.s.l.), a high-altitude urban environment on the Tibetan Plateau, during the spring and autumn observation periods. The specific aims are (i) to establish an event classification and to quantify the frequency and intensity of urban NPF, (ii) to elucidate the seasonal differences in precursor–meteorology interactions driving NPF, and (iii) to evaluate the instantaneous and seasonal enhancement of CCN concentrations attributable to newly formed particles at the TP urban environment. The observational methodology is described in Sect. 2, results and discussions are presented in Sect. 3, and conclusions together with implications for aerosol–climate interactions are summarized in the last section.

2 Methods

2.1 Sampling sites

As shown in Fig. 1, the study site is located at Tibet University (TU, 29°38′ N, 91°10′ E; 3650 m a.s.l.) in Lhasa, which lies in the south-central TP. Lhasa serves as the capital of the Tibet Autonomous Region and its political, economic, and cultural hub. As one of the largest urban centers on the TP, it is a typical high-altitude city where aerosols are predominantly driven by local sources, including traffic emissions, residential coal/biomass combustion, construction activities, and dust resuspension (Zhao et al., 2022). Traffic-related particle concentrations can exhibit pronounced spatial and temporal heterogeneity within complex urban environments, which may not be fully captured by fixed-site measurements (Yeganeh et al., 2026). This spatial heterogeneity should therefore be considered when interpreting the influence of local urban emissions at the TU site. The site is situated in a broad river valley surrounded by mountains with elevations up to 5500 m a.s.l. Its climate is strongly influenced by the Asian Summer Monsoon and the East Asian Winter Monsoon, with spring and autumn functioning as transitional seasons between these two climate systems (Li et al., 2025). In situ measurements were conducted during two periods: the autumn observation period (9 October–10 November 2024) and the spring observation period (25 March–22 April 2025).

2.2 Instrumentation

In this study, a comprehensive Scanning Mobility Particle Sizer (SMPS) system was employed to measure the PNSD from 3 to 800 nm with a 5 min time resolution. This system consisted of two separate instruments from TSI Inc. A nanoparticle SMPS (TSI, Model 3087) was used to measure particles in the size range of 3 to 40 nm, while a standard SMPS (TSI, Model 3080) measured particles from 20 to 800 nm. The two datasets were then merged to create a complete and continuous PNSD.

To ensure consistent and accurate measurements, the instruments were housed in a temperature-controlled container maintained at 25 °C. This setup was located on the rooftop of a campus building, with the aerosol inlet positioned approximately 20 m a.g.l. (above ground level). This elevated sampling height was chosen to minimize the influence of localized ground-level emission sources like traffic exhaust and suspended road dust. Furthermore, a silicon diffusion dryer was placed upstream of the SMPSs to reduce the relative humidity of the sampled air to below 40 %, preventing particle growth from water vapour condensation. Ambient aerosols were sampled through a short, conductive tube with minimal bends to reduce size-dependent diffusion losses. All SMPS data underwent rigorous corrections for these diffusion losses and for multiple charging effects to ensure the reliability of the measured particle number concentrations. We also utilized meteorological data from an on-site automatic weather station, which provided essential parameters including temperature (T), relative humidity (RH), wind speed (WS), wind direction (WD), Sulfur Dioxide (SO_2), Nitrogen Dioxide (NO_2), and Ozone (O_3) for a comprehensive analysis of the atmospheric conditions. Because gaseous H_2SO_4 was not directly measured, a relative H_2SO_4-related photochemical proxy was additionally calculated for periods with available spectral measurements during the autumn observation period; the calculation procedure and associated limitations are described in Sect. S1 in the Supplement.

2.3 Calculation of variables characterizing new particle formation

The Condensation Sink (CS, unit: s^{-1}) is utilized in this study as a core parameter to quantify the regulating effect of pre-existing aerosols on condensable vapors (Kerminen et al., 2018; Wu et al., 2021). Its calculation is based on the kinetic theory of dilute gases and assumes sulfuric acid (H_2SO_4) as the characteristic condensable substance (Dal Maso et al., 2005). The calculation process utilizes measured PNSD data and incorporates the influence of ambient temperature (T) and pressure (P). First, the diffusion coefficient of sulfuric acid vapor in the air ($D_{x,\mathrm{air}}$) is calculated using an empirical formula based on T and P. Subsequently, the mean free path of the condensable vapor (λ) is calculated using the molar mass of sulfuric acid ($M_x = 98.08\ \mathrm{g\ mol^{-1}}$). Based on λ and the size-resolved particle radius (R_i), the Knudsen number ($Kn_i = \lambda / R_i$) is determined. To correct the condensation rate from the continuous regime to the transition and free molecular regimes, the transition regime correction factor (β) is introduced (Dinoi et al., 2021):

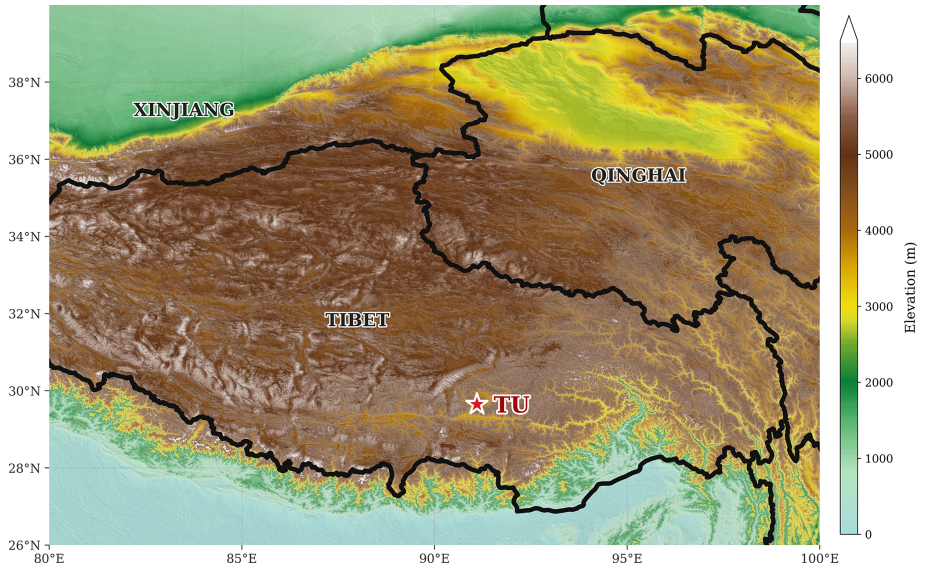

Figure 1. Regional topography and location of the Tibet University (TU) observation site in Lhasa, Tibet Autonomous Region, China. Color shading denotes elevation above sea level (m), black lines indicate provincial-level administrative boundaries, and the red star marks the TU observation site.

$$\beta = \frac{Kn + 1}{0.377Kn + 1 + \frac{4}{3\alpha}\left(Kn^2 + Kn\right)}. \quad (1)$$

Here, the sticking coefficient (α) is set to 1.0. Finally, the size-resolved condensation sink (CSi) is determined by $4\pi \cdot D_{x,\mathrm{air}} \cdot R_i \cdot \beta i \cdot n_i$, and the total CS value is quantitatively calculated by numerically integrating CSi over all particle size ranges.

$$\mathrm{CS} = 2\pi D \int_0^\infty d_\mathrm{p}\beta_\mathrm{m}\left(d_\mathrm{p}\right) \times n\left(d_\mathrm{p}\right) dd_\mathrm{p} = 2\pi D \sum_i \beta_i d_{\mathrm{p}_i} N_i. \quad (2)$$

The Coagulation Sink (CoagS, unit: s^{-1}) is another key parameter in atmospheric aerosol dynamics, quantifying the efficiency of pre-existing particles (scavenger particles) in removing specific size-range target particles from the system via the coagulation mechanism (Kulmala et al., 2001). Similar to CS, CoagS is calculated through PNSD integration.

$$\mathrm{CoagS}_{d_\mathrm{p}} = \int K\left(d_p, d_{\mathrm{p}'}\right) n\left(d_{\mathrm{p}'}\right) dd_{\mathrm{p}'} \cong \sum_{d_{\mathrm{p}'}=d_\mathrm{p}}^{d_{\mathrm{p}'}=\max} K\left(d_\mathrm{p}, d_{\mathrm{p}'}\right) N_{\mathrm{d}_{\mathrm{p}'}} \quad (3)$$

GR, defined as the rate at which the geometric mean diameter of nucleation mode particles increases from d_{p_1} to d_{p_2}, was calculated using the procedure outlined by (Kulmala et al., 2012).

$$\mathrm{GR} = \frac{\Delta d_\mathrm{p}}{\Delta t} = \frac{d_{\mathrm{p}_2} - d_{\mathrm{p}_1}}{t_2 - t_1} \quad (4)$$

To quantify the intensity of NPF events, we calculated the particle formation rate J (i.e., the rate of aerosol particle formation at a specific size) following the method described by Baalbaki et al. (2021), which is derived from rearranging the equation governing the time evolution of particle number concentration (Kulmala et al., 2012). Specifically, J was computed for two size bins (d_p): 3 nm (J_3), and 7 nm (J_7), with the upper size limits of the corresponding bins set to 7 and 20 nm, respectively. The growth rate term in the equation (Eq. 5) was defined as the average of GR measurements for total particles; this GR value was assumed constant during NPF events and set to zero outside the event duration or in non-event periods. The formation rate J_{d_p} is expressed as:

$$J_{d_\mathrm{p}} = \frac{\mathrm{d}N_{d_\mathrm{p}}}{\mathrm{d}t} + \mathrm{CoagS}_{d_\mathrm{p}} \cdot N_{d_\mathrm{p}} + \frac{\mathrm{GR}}{\Delta d_\mathrm{p}} \cdot N_{d_\mathrm{p}}. \quad (5)$$

CCN concentration is quantitatively calculated based on κ–Köhler theory (Petters and Kreidenweis, 2007). This method aims to determine the number of particles that can be activated at a specific supersaturation (S).

$$A = \frac{4\sigma_{\mathrm{s/a}} M_\mathrm{w}}{RT\rho_\mathrm{w}} \quad (6)$$

$$\kappa = \frac{4A^3}{27D_\mathrm{c}^3 \ln^2 S_\mathrm{c}}. \quad (7)$$

In Eqs. (6) and (7), D_c is the critical dry particle diameter for CCN activation, S_c is the critical saturation ratio, and A is the Kelvin term. The parameter κ represents the influence of particle chemical composition on hygroscopicity and solution water activity. $\sigma_{\mathrm{s/a}}$ is the surface tension of water against air. M_w and ρ_w are the molar mass and density of water, respectively. R is the universal gas constant, and T is the absolute

temperature (K). In this study, κ and S were set to 0.12 and 1.2 %, respectively.

2.4 NPF event classification

In this study, atmospheric particles were divided into three diameter modes: the nucleation mode (< 25 nm), the Aitken Mode (25–100 nm), and the accumulation mode (> 100 nm) (Wang et al., 2022; Hussein et al., 2020; Kalkavouras et al., 2021; Shen et al., 2022). The classification followed the methodology proposed by Dal Maso et al. (2005), which has been widely applied in previous NPF studies (Gao et al., 2025; Cramer et al., 2026; Lampilahti et al., 2025; Casans et al., 2025). Based on visual inspection of the daily PNSD evolution, the observation days were classified as NPF days, Undefined days, or Non-Event days. The classification was further supported by size-segregated particle number concentrations and candidate particle growth rates.

NPF days were characterized by the appearance of a distinct new particle mode at small diameters followed by identifiable growth toward larger sizes. Continuous growth throughout the entire day was not required because temporary interruptions may result from changes in air masses, boundary-layer development, precursor availability, or missing measurements. All remaining days were treated as non-NPF days and further divided into Undefined and Non-Event days. Undefined days showed increases in small-particle concentrations or partial modal evolution, but the formation and growth patterns were too weak, discontinuous, or ambiguous to be confidently classified as NPF. Non-Event days showed neither the distinct appearance of a new particle mode nor its subsequent systematic growth. To improve the transparency of the classification, the mean $N_{3–25}$ and $N_{2–100}$ concentrations during 09:00-18:00 local time and candidate $GR_{7–20}$ values derived from continuous growth trajectories within 07:00-18:00 LT were included as supporting metrics. These metrics were used to support the day-by-day classification rather than as fixed classification thresholds. The revised classification, event timing, particle number characteristics, and candidate $GR_{7–20}$ values for individual observation days are provided in Table S1 in the Supplement. Daily PNSD plots for NPF, Undefined, and Non-Event days are presented in Figs. S1–S3 in the Supplement. The former Class I and Class II categories were merged into the NPF-day category for all main statistical analyses, while the original classification is retained in Table S1 only for comparison and traceability.

Figure 2 presents representative dates for the NPF, Undefined, and Non-Event categories. Figure 2a shows their diurnal PNSD evolution. On the NPF day, the number concentration of small particles began to increase at approximately 09:00 LT, followed by an identifiable shift of the particle mode from the nucleation mode toward the Aitken mode, forming the characteristic "banana-shaped" pattern. On the Undefined day, the modal evolution was relatively weak, discontinuous, or ambiguous. On the Non-Event day, no distinct formation of a new particle mode followed by systematic growth was observed. Figure 2b shows the corresponding mean PNSD and modal fitting results for the nucleation mode, Aitken mode, and accumulation mode. The NPF day was characterized by substantial contributions from both the nucleation mode and Aitken mode, consistent with the formation and subsequent growth of newly formed particles. The Undefined day was dominated by particles in the nucleation mode but showed relatively limited development toward larger sizes, whereas the Non-Event day exhibited greater relative contributions from pre-existing particles in the Aitken mode and accumulation mode. Figure 2c shows the relative contributions of the three particle modes. On the NPF day, particles in the nucleation mode, Aitken mode, and accumulation mode contributed 42 %, 57 %, and 1 % of the total particle number concentration, respectively, consistent with the growth of newly formed particles toward the Aitken mode. On the Undefined day, the corresponding contributions were 77 %, 20 %, and 3 %, respectively, indicating that particles in the nucleation mode dominated but their subsequent growth remained limited or ambiguous. On the Non-Event day, the corresponding contributions were 12 %, 56 %, and 32 %, respectively, reflecting greater relative contributions from pre-existing particles in the Aitken mode and accumulation mode.

3 Results and discussion

3.1 Overview of the field observations

Meteorological conditions and gaseous pollutants exhibited strong short-term fluctuations and clear diurnal variability during both measurement periods. As shown in Fig. 3a and b, WS, WD and RH varied substantially on synoptic and diurnal timescales. The autumn observation period was characterized by higher RH (42 ± 18 %; median: 39 %) than the spring observation period (28 ± 18 %; median: 23 %). Wind speeds were comparable between the two periods (arithmetic mean $\pm$ standard deviation: 1.6 ± 0.9 and 1.9 ± 1.1 m s^{-1}; median: 1.4 and 1.7 m s^{-1} for the autumn and spring observation periods, respectively), indicating predominantly low-to-moderate ventilation conditions that may facilitate episodic accumulation of precursors and aerosols. Figure 3c and d presents the temporal evolution of SO_2, CS, O_3, and NO_2. O_3 was generally higher during the spring observation period (52 ± 14 ppb; median: 55 ppb) than during the autumn observation period (38 ± 13 ppb; median: 39 ppb), suggesting a more oxidizing background in the spring observation period. In contrast, SO_2 and NO_2 showed intermittent spikes in both observation periods, implying episodic impacts from transport and/or local emissions. Notably, the CS remained similar across observation periods, with values of $(7.9 \pm 5.3) \times 10^{-3}$ s^{-1} (median: 6.5×10^{-3} s^{-1}) in the autumn observation period and $(8.1 \pm 3.8) \times 10^{-3}$ s^{-1} (median:

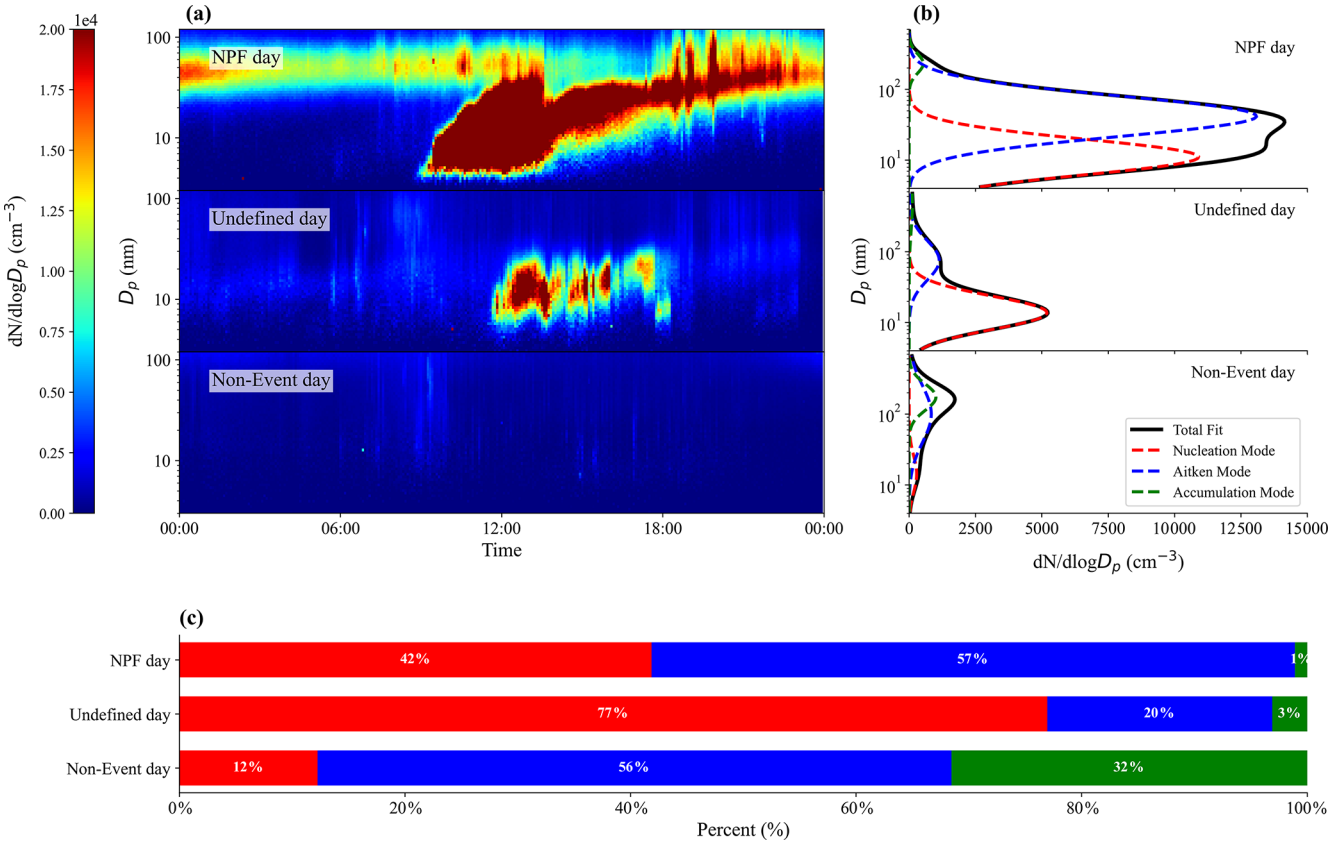

Figure 2. **(a)** Particle number size distribution evolution, **(b)** averaged modal fitting, and **(c)** relative number contributions for three day categories.

7.2×10^{-3} s^{-1}) in the spring observation period, indicating that the observation-period difference in NPF occurrence is unlikely driven solely by differences in the pre-existing particle sink.

NPF events were frequently observed at the TU site and were associated with pronounced differences between the two observation periods in PNSD and estimated CCN concentrations. In total, 43 NPF events, 6 Undefined days, and 9 Non-Event days were identified during the 58 measurement days. The autumn observation period included 25 NPF days, 1 Undefined day, and 3 Non-Event days, whereas the spring observation period included 18 NPF days, 5 Undefined days, and 6 Non-Event days. Based on Fig. 3g, NPF occurrence displayed a marked observation-period contrast, with NPF observed on 86.2 % of the measurement days during the autumn observation period but only on 62.1 % during the spring observation period. Figure 3e shows that the total particle number concentration ($N_{3–700}$) was substantially higher during the autumn observation period, with an arithmetic mean ± standard deviation of $(10.5 \pm 9.8) \times 10^3$ cm^{-3} and a median of 7.1×10^3 cm^{-3}, than during the spring observation period, when the corresponding values were $(5.3 \pm 6.8) \times 10^3$ and 2.9×10^3 cm^{-3}, respectively. The median particle diameter (median D_p) was smaller during the autumn observation period, with an arithmetic mean ± standard deviation of 37 ± 14 nm and an observation-period median of 39 nm, than during the spring observation period, when the corresponding values were 45 ± 34 and 38 nm, respectively. This difference indicates a stronger contribution from smaller particles during the autumn observation period. Figure 3f further presents the estimated CCN concentrations and the fractional contributions from different modes. Estimated CCN concentrations were higher during the autumn observation period, with an arithmetic mean ± standard deviation of $(2.8 \pm 1.7) \times 10^3$ cm^{-3} and a median of 2.4×10^3 cm^{-3}. These higher concentrations were accompanied by more frequent and persistent enhancements in the nucleation- and Aitken-mode fractions and episodic reductions in the accumulation-mode fraction, suggesting a shift of the particle population toward the small-to-intermediate size range. In contrast, the spring observation period showed a lower arithmetic mean ± standard deviation estimated CCN concentration of $(1.2 \pm 0.6) \times 10^3$ cm^{-3} and a median of 0.96×10^3 cm^{-3}, together with weaker and less persistent increases in the nucleation- and Aitken-mode fractions and a more dominant background contribution from the accumulation mode. Together, these observations highlight strong observation-period differences of particle sources and CCN-relevant size

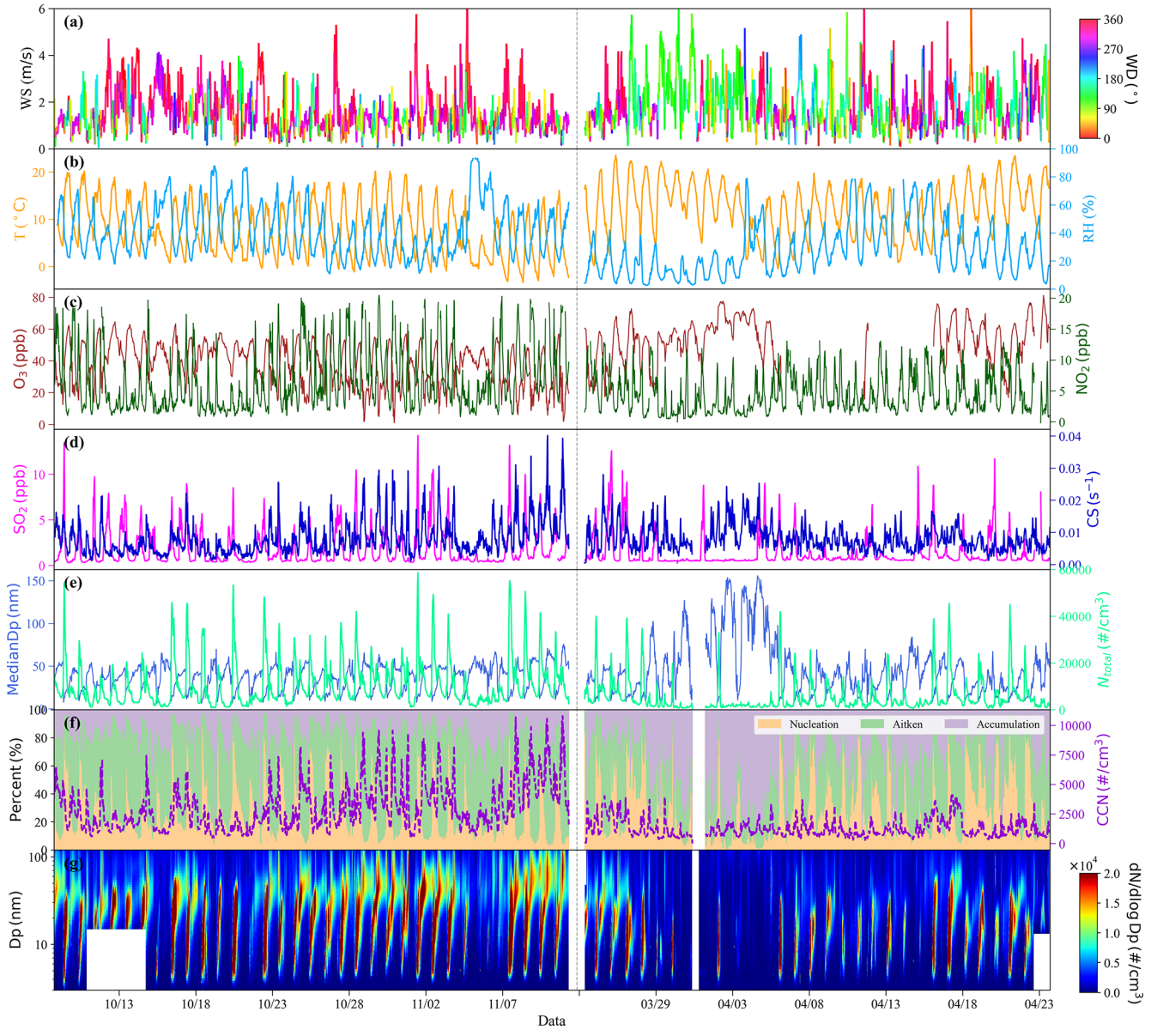

Figure 3. Time series of **(a)** wind speed and wind direction, **(b)** ambient temperature and relative humidity, **(c)** O_3 concentration and NO_2 concentration, **(d)** SO_2 concentration and Condensation Sink, **(e)** median particle diameter and particle number concentration in the size range of 3–700 nm, **(f)** CCN concentration and percentage contributions of the nucleation mode, Aitken mode, and accumulation mode, **(g)** PNSD during the spring and autumn observation periods.

structure at the TU site and provide context for the process-based analysis in the following sections.

3.2 PNSD and number concentration responses

3.2.1 Mean PNSD and modal contributions

The mean PNSD and modal contributions reveal clear differences in the campaign-mean particle size structure and surface-area/volume partitioning between the autumn and spring observation periods. Figure 4a shows that the mean PNSD during the two observation periods at the TU site was typically multimodal, reflecting the combined influences of secondary particle production, particle growth, and the pre-existing aerosol population. The total particle number concentration differed markedly between the two observation periods. The arithmetic mean ± standard deviation of $N_{3–700}$ was $(10.5 \pm 9.8) \times 10^3$ cm^{-3} during the autumn observation period and $(5.3 \pm 6.8) \times 10^3$ cm^{-3} during the spring observation period, with the former being approximately 2.0 times higher than the latter (Fig. 4a). In terms of modal partitioning, Fig. 4b indicates that while the Aitken mode dominates

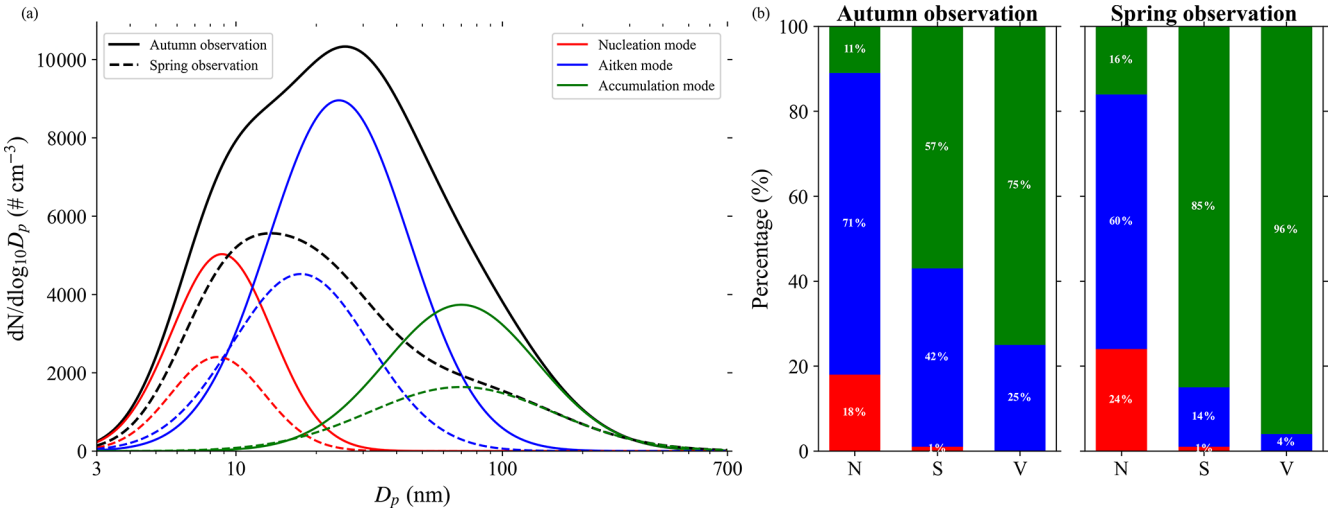

Figure 4. **(a)** Particle number size distribution characteristics and **(b)** modal contributions to number (N), surface area (S), and volume (V) distributions during the spring and autumn observation periods.

number concentration in both periods, the surface area and volume are strongly controlled by the accumulation mode in the spring observation period, accounting for 85 % (surface area) and 96 % (volume). In contrast, during the autumn observation period the Aitken mode contributes substantially more to surface area (42 %) and volume (25 %) than in thespring observation period (14 % and 4 %, respectively), consistent with a particle population shifted toward smaller-to-intermediate sizes. These differences between the two observation periods provide a baseline for interpreting event-day diurnal changes and their implications for CCN-relevant size fractions.

3.2.2 Diurnal variations of size-segregated number concentrations

The diurnal profiles of size-segregated particle number concentrations differed clearly among NPF, Undefined, and Non-Event days. Figure 5 summarizes diurnal profiles of particle number concentrations for the nucleation mode ($N_{3–25}$), Aitken mode ($N_{25–100}$), accumulation mode ($N_{100–700}$), and total measured size range ($N_{3–700}$) across the three day categories. On NPF days, $N_{3–25}$ increased rapidly during the morning, reached a pronounced maximum at approximately 11:00–12:00 LT, and subsequently declined (Fig. 5a). Undefined days exhibited a weaker and broader increase from late morning to afternoon, whereas Non-Event days maintained substantially lower $N_{3–25}$ concentrations without a preceding $N_{3–25}$ peak. $N_{3–700}$ showed a similar pattern, with the highest and most pronounced daytime maximum occurring on NPF days (Fig. 5b). $N_{25–100}$ on NPF days exhibited a broad daytime enhancement from approximately 11:00 to 15:00 LT, followed by a secondary increase in the evening (Fig. 5c). The daytime enhancement is consistent with the growth of newly formed particles into the Aitken mode, whereas the evening increase may also be influenced by local urban emissions. Undefined days showed relatively weak variations in $N_{25–100}$, while Non-Event days exhibited a more evident evening increase without a preceding increase in the nucleation mode. Differences in $N_{100–700}$ among the three categories were relatively small, although modest morning and evening enhancements were observed (Fig. 5d). These diurnal statistics indicate that the impact of NPF on the size distribution depends not only on daytime particle production, but also on the persistence of growth into the Aitken mode.

3.3 Factors controlling the formation and development of NPF events

3.3.1 Formation and growth characteristics

Figure 6 summarizes the diurnal variations in particle formation rates at 3 nm (J_3) and 7 nm (J_7) for the three day categories. On NPF days, both formation rates increased rapidly during the morning and reached pronounced maxima at approximately 09:00–11:00 LT, followed by a gradual decline. Undefined days exhibited weaker and less persistent daytime enhancements, whereas Non-Event days generally showed the lowest formation-rate signals and lacked a distinct morning peak. These contrasting diurnal patterns support the occurrence of active daytime particle formation on NPF days.

During 08:00–16:59 LT, the mean J_3 and J_7 on NPF days were 1.2 ± 2.0 and $2.2 \pm 3.3\,\mathrm{cm^{-3}\,s^{-1}}$, respectively, with corresponding median values of 0.44 and $1.12\,\mathrm{cm^{-3}\,s^{-1}}$. The observed J_3 was of the same order of magnitude as the formation rates reported at Nam Co ($J_4 = 1.2 \pm 0.6\,\mathrm{cm^{-3}\,s^{-1}}$) (Tang et al., 2023) and the Mt. Yulong station (J_3: $1.2\,\mathrm{cm^{-3}\,s^{-1}}$) (Shang et al., 2018). The arithmetic mean ± standard deviation values of $GR_{3–7}$ and $GR_{7–20}$ were

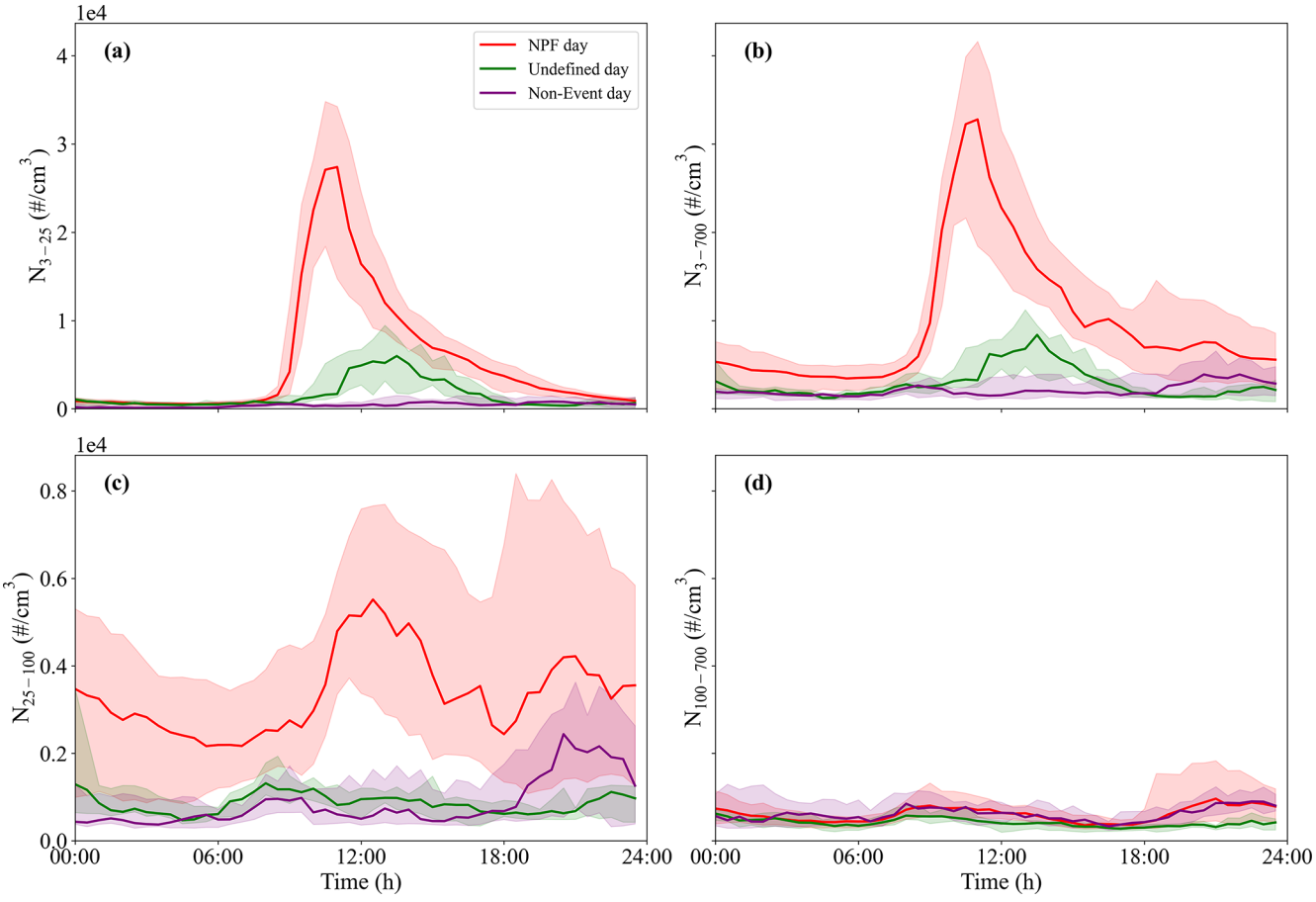

Figure 5. Diurnal variation of aerosol number concentrations (# cm^{-3}) at the size ranges of **(a)** 3–25 nm, **(b)** 3–700 nm, **(c)** 25–100 nm, and **(d)** 100–700 nm, on NPF, Undefined, and Non-Event days. Shaded areas represent the interquartile range (25th to 75th percentiles).

3.7±1.1 and 2.0±1.7 nm h^{-1}, respectively, with corresponding median values of 3.6 and 1.3 nm h^{-1}. These growth rates were broadly comparable to values at Nam Co ($GR_{4–25}$: 4.0± 1.2 nm h^{-1}) and Mt. Yulong (3.2 nm h^{-1}), but higher than the value reported at the NCO-P station (1.2±0.7 nm h^{-1}) (Venzac et al., 2008). In summary, the J and GR values at TU are well within the ranges reported for global high-altitude environments, indicating that the site experiences characteristic high-altitude NPF with strong daytime formation and sufficiently rapid growth to promote downstream enhancement of Aitken-mode number concentrations.

3.3.2 Condensation sink and its role

CS represents the ability of the pre-existing aerosol population to remove condensable vapors via condensation, while CoagS describes the loss of freshly formed clusters and ultrafine particles through collision and coalescence with larger background particles (Victor et al., 2024). Figure 7 shows the diurnal variations of CS and CoagS for different day types and observation periods. Both sink terms exhibit clear diurnal structure and substantial variability, indicating that the removal capacity for vapors and nascent particles can change markedly over the course of a day and between different regimes.

Consistent with many studies reporting that NPF tends to be favored under relatively low CS (Cai et al., 2017; Saha et al., 2018; Kalivitis et al., 2019; Kalkavouras et al., 2020; Aktypis et al., 2023), the TU site nevertheless shows that NPF can occur even when CS is not minimal. The mean CS levels (±1σ) were (6.9 ± 4.5) × 10^{-3} s^{-1} on NPF days, (5.1 ± 4.3)×10^{-3} s^{-1} on Undefined days, and (6.4±4.4)×10^{-3} s^{-1} on Non-Event days (Fig. 7a–c), with corresponding median values of 5.8 × 10^{-3}, 3.5 × 10^{-3}, and 5.0 × 10^{-3} s^{-1}. Thus, CS on NPF days was slightly higher than that on Non-Event days, and the NPF-day mean CS at TU is higher than values reported for remote plateau background sites in China (Tang et al., 2023), yet lower than those reported for the major urban environment of Beijing (Du et al., 2017), suggesting an intermediate sink environment characteristic of a high-altitude urban setting. Moreover, the mean CS values were broadly similar between the autumn and spring observation periods, at (6.9 ± 4.1) × 10^{-3} and (6.2 ± 4.7) × 10^{-3} s^{-1}, respectively, with corresponding median values of 5.9 × 10^{-3}

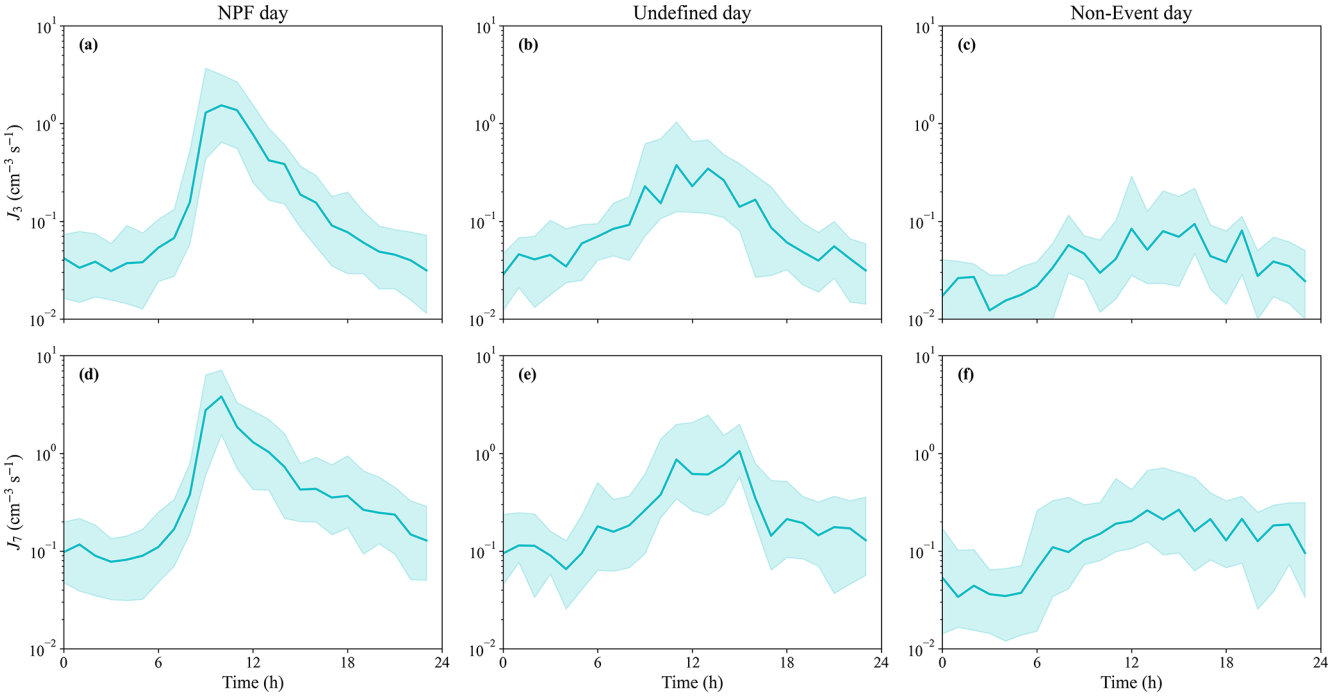

Figure 6. Diurnal variations of the formation rates J_3 during **(a)** NPF day, **(b)** Undefined day, and **(c)** Non-Event day periods. The corresponding diurnal variations of the formation rate J_7 are shown in panels **(d)**–**(f)**. The shaded areas represent the 25th and 75th percentile boundaries, and the solid lines denote the median values.

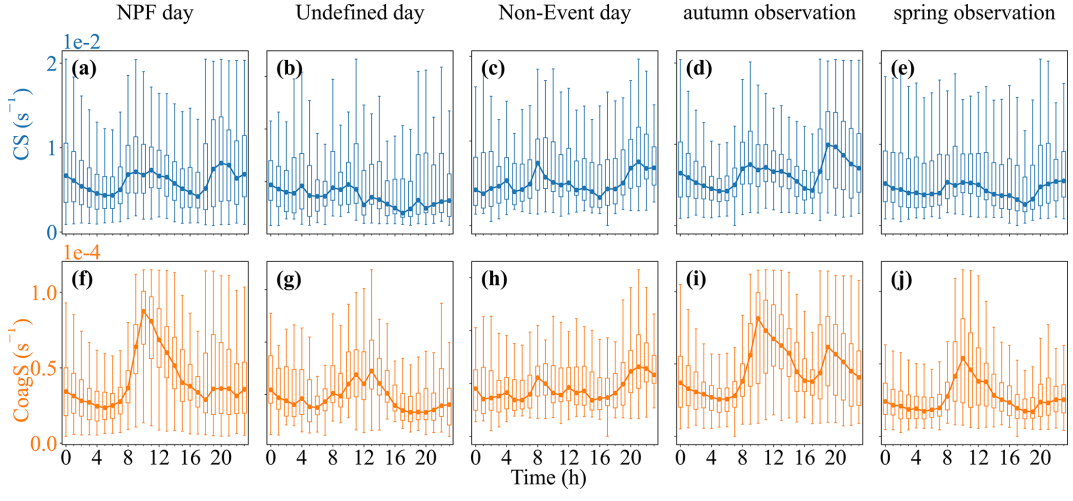

Figure 7. Diurnal variations of condensation sink and coagulation sink for different event classifications and observation periods.

and 4.5×10^{-3} s^{-1} (Fig. 7d and e). Therefore, differences in the pre-existing particle sink were unlikely to be the primary explanation for the contrast in NPF frequency between the two observation periods.

In contrast, CoagS shows a stronger separation among day types and observation periods. The mean CoagS values were $(4.3 \pm 2.6) \times 10^{-5}$ s^{-1} on NPF days, $(2.2 \pm 1.2) \times 10^{-5}$ s^{-1} on Undefined days, and $(2.5 \pm 1.4) \times 10^{-5}$ s^{-1} on Non-Event days, with corresponding median values of 3.6×10^{-5}, 1.9×10^{-5}, and 2.2×10^{-5} s^{-1}, respectively (Fig. 7f–h). The mean CoagS was also higher during the autumn observation period $(4.5 \pm 2.6) \times 10^{-5}$ s^{-1} than during the spring observation period $(2.9 \pm 2.0) \times 10^{-5}$ s^{-1}, with corresponding median values of 3.9×10^{-5} and 2.4×10^{-5} s^{-1}, respectively (Fig. 7i and j). Because CoagS reflects the scavenging loss of newly formed clusters and ultrafine particles, its elevated value during the autumn observation period indicates a stronger constraint on particle survival. However, NPF occurred more frequently

during this period, suggesting that particle-production processes were sufficiently strong to offset the enhanced coagulation loss.

Taken together, these results suggest that the occurrence and development of NPF at TU are better interpreted as the outcome of competition between particle-production and loss processes rather than as being controlled by the sink alone. This interpretation is consistent with previous observations that NPF can be observed under moderate sinks when vapor production is sufficiently strong (Zhang et al., 2021; Sellegri et al., 2019; Wang et al., 2022; Baalbaki et al., 2021). In this framework, CoagS provides an additional constraint on whether newly formed clusters can survive long enough to grow into larger sizes, while CS limits the availability of low-volatility vapors required for sustained growth; hence, event intensity and downstream impacts are expected to depend on the joint evolution of formation/growth rates and sinks over the diurnal cycle.

3.3.3 Meteorology and precursor modulation, with transport context

Meteorological conditions during the study period exhibited clear diurnal variability, consistent with the dependence of NPF on atmospheric state and precursor availability reported in previous studies (Hakala et al., 2022; Kalkavouras et al., 2019, 2020; Victor et al., 2024; Singh et al., 2025). The site was predominantly under clear to partly cloudy conditions with sufficient solar radiation, occasionally interrupted by precipitation. Notably, an extended rainfall episode occurred from 5 to 6 November during the autumn observation period, during which no NPF events were identified. The absence of NPF during this episode may have been associated with wet scavenging and reduced photochemical production of condensable vapors under rainy and cloudy conditions.

To examine the associations of meteorological conditions and key gaseous precursors with NPF, we compared SO_2, O_3, and NO_2, together with temperature, RH, and wind speed, across day types and between the two observation periods. As described in Sect. 3.1, the spring observation period was warmer and slightly windier, whereas the autumn observation period was more humid. The comparatively weaker ventilation during the autumn observation period may have favored the episodic accumulation of gaseous precursors and particles.

During the autumn observation period, SO_2 and NO_2 mixing ratios were higher on NPF days than on non-NPF days. The mean SO_2 mixing ratio was 1.9 ± 2.0 ppb on NPF days and 0.7 ± 0.7 ppb on non-NPF days, with corresponding median values of 0.9 and 0.5 ppb, respectively. The mean NO_2 mixing ratios were 7.2 ± 4.9 and 4.6 ± 3.9 ppb, with corresponding median values of 5.9 and 3.2 ppb, respectively. Wind-sector analysis further showed that elevated SO_2 and NO_2 mixing ratios occurred more frequently under southerly winds on NPF days, whereas generally lower values were observed in the corresponding sectors on non-NPF days (Fig. 8). Because SO_2 oxidation by OH• produces H_2SO_4, and H_2SO_4 is widely recognized as a key nucleation precursor and critical for early particle growth, the higher SO_2 concentrations observed on NPF days suggest that sulfur-containing precursors may have played an important role in NPF during the autumn observation period (Olin et al., 2020; Yao et al., 2018; Kerminen et al., 2018). Although elevated NO_2 can alter atmospheric radical chemistry and potentially reduce OH availability under some conditions, the clearly elevated SO_2 observed on NPF days suggests that plentiful SO_2 increases the potential for H_2SO_4 formation. This interpretation is further supported by Fig. S4, which shows that during the particle-formation period SO_2 concentrations on NPF days are clearly higher than those on non-NPF days. Moreover, for periods with available spectral measurements, the relative H_2SO_4-related proxy was also higher on NPF days during the particle-formation period (Fig. S5), providing additional evidence for an association between photochemical H_2SO_4 production and autumn NPF. These results suggest that the increased availability of sulfur-containing precursors may have partly compensated for potentially unfavorable effects associated with elevated NO_x and supported NPF occurrence (Gao et al., 2025). Although the proxy is not a direct measurement of H_2SO_4, these results support an important contribution from sulfur-containing precursors to autumn NPF rather than demonstrating their exclusive control.

During the spring observation period, no single, well-defined factor controlling NPF occurrence was evident. As shown in Figs. 9 and S6, SO_2, NO_2, and O_3 exhibited differences between NPF and non-NPF days during certain hours and under specific wind conditions. However, no consistent separation between the two categories was observed across all gaseous species or throughout the particle-formation period. Wind speed and wind direction likewise did not show a distinctive pattern that consistently characterized NPF days. These results suggest that spring NPF was more likely associated with the combined effects of multiple processes, including precursor availability, atmospheric oxidation, and boundary-layer evolution, rather than with any single dominant factor (Wu et al., 2024). Given the relatively weak and inconsistent contrasts in the measured inorganic gaseous precursors, a contribution from VOC-related oxidation processes cannot be excluded, particularly for the subsequent growth of newly formed particles (Zhang et al., 2026; Yang et al., 2026). However, because direct observations of VOCs and their oxidation products are not available in this study, their specific role cannot be further constrained and still requires additional investigation.

Overall, the comparison between the two observation periods indicates differences in the factors associated with NPF, although the relatively short measurement periods preclude establishing a general seasonal pattern. During the autumn observation period, NPF was associated with higher

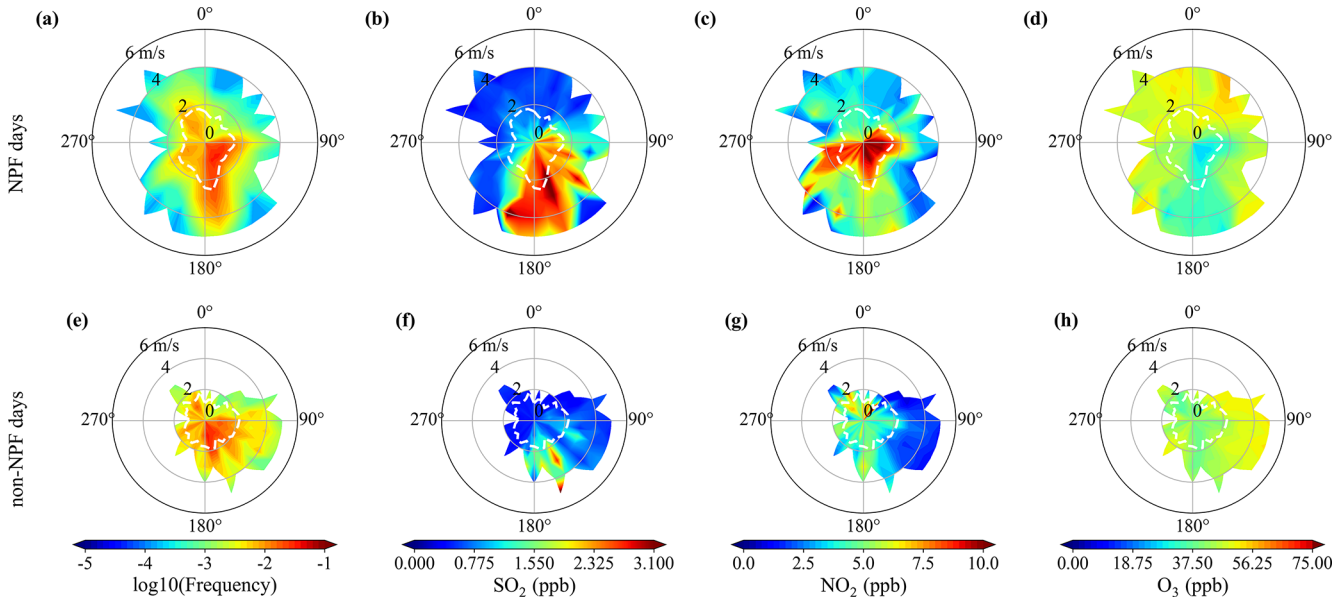

Figure 8. Wind-sector analysis comparing the distributions of **(a)** wind speed and wind direction frequency together with sector-averaged concentrations of **(b)** SO_2, **(c)** NO_2, and **(d)** O_3, for NPF days during the autumn observation period; panels **(e)–(h)** show the corresponding wind-sector frequency and gas concentrations for non-NPF days during the autumn observation period.

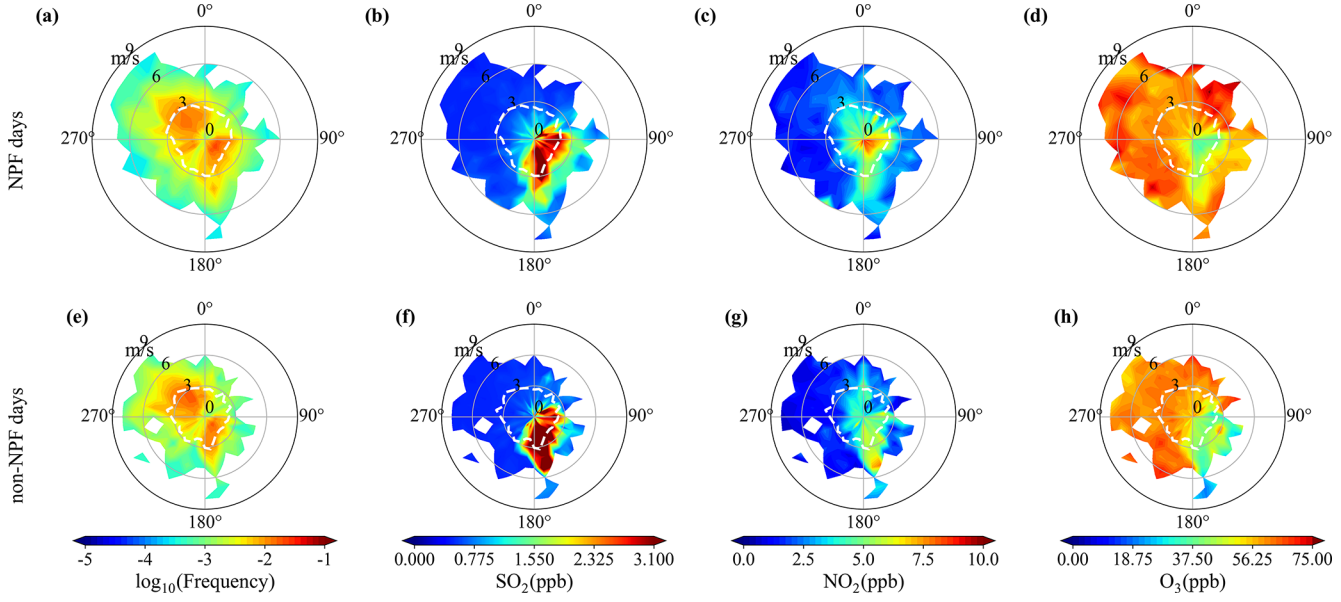

Figure 9. Wind-sector analysis comparing the distributions of **(a)** wind speed and wind direction frequency together with sector-averaged concentrations of **(b)** SO_2, **(c)** NO_2, and **(d)** O_3, for NPF days during the spring observation period; panels **(e)–(h)** show the corresponding wind-sector frequency and gas concentrations for non-NPF days during the spring observation period.

SO_2 concentrations and an enhanced relative H_2SO_4-related proxy during the particle-formation period, suggesting an important contribution from sulfur-containing precursors rather than demonstrating a uniquely sulfur-precursor-driven regime. Elevated NO_2 may have modified atmospheric radical chemistry, but its net effect on NPF could not be determined from the available measurements. In contrast, during the spring observation period, no single dominant factor was identified. Instead, precursor availability, atmospheric oxidation, boundary-layer evolution, and potentially VOC-related oxidation may have jointly affected particle formation and growth. Because H_2SO_4, ammonia, amines, VOCs, and their oxidation products were not directly measured, their respective contributions could not be quantified, and the detailed

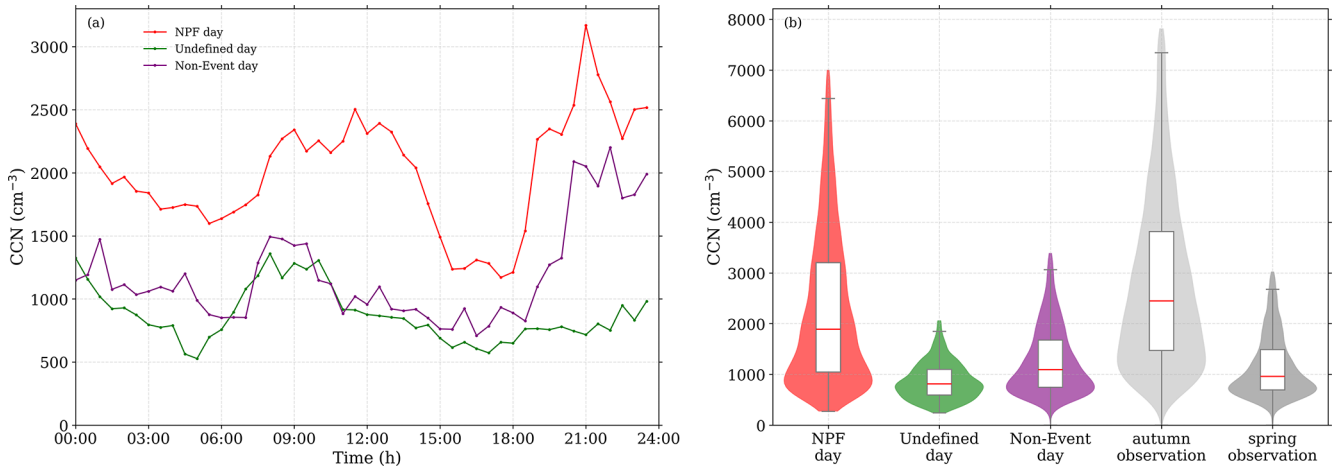

Figure 10. **(a)** Diurnal variations and **(b)** statistical distributions of estimated CCN concentrations for NPF, Undefined, and Non-Event days and for the autumn and spring observation periods. CCN concentrations were estimated using $\kappa = 0.12$ and $S = 1.2\,\%$.

molecular mechanisms during both observation periods remain uncertain.

3.4 Modulation of CCN by NPF in urban air

To quantify the influence of NPF on CCN in the urban atmosphere of the Tibetan Plateau, we examined both the diurnal evolution and the distribution of estimated CCN for different event categories as well as for the two periods (spring and autumn). Because direct measurements of CCN concentration were unavailable in this study, CCN was estimated from the measured PNSD using the κ–Köhler framework described in Sect. 2.3, assuming a constant particle hygroscopicity parameter κ of 0.12 and a supersaturation S of 1.2 %. Because the estimated CCN concentrations depend on these assumptions, a sensitivity analysis was conducted using κ values of 0.08, 0.12, and 0.20 and supersaturations of 0.6 %, 0.8 %, and 1.2 % (Fig. S7). Although the absolute CCN concentrations varied with κ and S, estimated CCN remained consistently higher during the autumn observation period than during the spring observation period across the tested parameter combinations.The estimated CCN concentrations were higher than $N_{100–700}$, because the assumed κ and supersaturation corresponded to a critical activation diameter below 100 nm, allowing part of the Aitken-mode particle population to contribute to the estimated CCN.

Figure 10a shows clear differences in the diurnal variation of estimated CCN concentrations among NPF, Undefined, and Non-Event days. NPF days generally exhibited the highest CCN concentrations, with pronounced daytime variations and a marked enhancement during the late afternoon and evening. This late-day enhancement is consistent with the continued growth and survival of newly formed particles into CCN-relevant sizes (Shen et al., 2019). Undefined days showed the lowest CCN concentrations and relatively weak diurnal variability. Non-Event days generally exhibited intermediate CCN concentrations, including an evening increase that may reflect the influence of pre-existing particles and local urban emissions rather than daytime NPF. The distributions in Fig. 10b likewise show that estimated CCN concentrations were generally higher and more broadly distributed on NPF days than on Undefined and Non-Event days. To further examine the role of particle growth, NPF days were divided into high- and low-$N_{25–100}$ groups using the observation-period-specific median of daily mean $N_{25–100}$ during 09:00–18:00 LT. The high-$N_{25–100}$ group exhibited higher estimated CCN concentrations, particularly in the afternoon and evening (Fig. S8), supporting the importance of continued particle growth and survival for potential CCN production.

The distributions in Fig. 10b show substantially higher estimated CCN concentrations during the autumn observation period than during the spring observation period. The median (interquartile range) estimated CCN concentration was 2.4×10^3 cm^{-3} ($1.5 - -3.8 \times 10^3$ cm^{-3}) during the autumn observation period, with an arithmetic mean $\pm$ standard deviation of $(2.8 \pm 1.7) \times 10^3$ cm^{-3}. During the spring observation period, the corresponding median was 0.96×10^3 cm^{-3} ($0.70–1.5 \times 10^3$ cm^{-3}), and the arithmetic mean $\pm$ standard deviation was $(1.2 \pm 0.6) \times 10^3$ cm^{-3}. These differences coincided with the higher NPF frequency during the autumn observation period and suggest that frequent NPF, together with subsequent particle growth, may have contributed to the higher estimated CCN-relevant particle concentrations at the TU site.

Overall, our results indicate that NPF days were associated with higher estimated CCN concentrations in the TP urban atmosphere, although the magnitude of the estimates depended on the assumed κ and supersaturation. The pronounced late-day enhancement on NPF days, particularly in the high-$N_{25–100}$ group, highlights the importance of sus-

tained post-formation growth and particle survival in determining the potential CCN response. At the observation-period scale, the higher estimated CCN concentrations during the autumn observation period may reflect the combined influence of frequent NPF and favorable particle-growth conditions. Because CCN concentrations were estimated rather than directly measured, these results indicate potential CCN production rather than direct confirmation of CCN activation.

4 Conclusion

This study provides a comprehensive characterization of NPF in Lhasa, a high-altitude urban center on the Tibetan Plateau, with particular emphasis on the controlling factors of NPF and its implications for CCN during the spring and autumn observation periods. Frequent NPF was observed throughout the campaigns. The contrast between the two observation periods in NPF occurrence was pronounced, with event frequencies of 86.2 % during the autumn observation period and 62.1 % during the spring observation period, indicating that the NPF regime in Lhasa is highly sensitive to variations in meteorology and atmospheric chemistry between the observation periods.

The results indicate that differences in the pre-existing particle sink alone cannot explain the contrast in NPF frequency between the two observation periods, and that precursor availability and atmospheric oxidation likely also played important roles. The CS remained comparable between the two observation periods, suggesting that the observed contrast in NPF frequency cannot be explained by sink suppression alone. Instead, the chemical–meteorological context differs substantially across observation periods. During the autumn observation period, NPF days were associated with elevated SO_2 and a higher relative H_2SO_4-related proxy during the particle-formation period, suggesting that sulfur-containing precursors likely contributed to particle formation and early growth. In contrast, the spring observation period NPF did not show a single, well-defined controlling factor, but was more likely influenced by the combined effects of precursor supply, atmospheric oxidation, and boundary-layer evolution. Under such conditions, VOC-related oxidation may contribute to the early growth of newly formed particles, although its specific role remains to be further constrained.

A key outcome of this work is that NPF days were associated with higher estimated CCN concentrations in Lhasa, and that the potential CCN response depended critically on whether newly formed particles continued to grow and survive after formation. Estimated CCN concentrations were generally higher on NPF days than on Undefined and Non-Event days. Moreover, NPF days with higher $N_{25–100}$ exhibited greater afternoon and evening CCN enhancements than those with lower $N_{25–100}$, supporting the importance of continued particle growth and survival in determining whether newly formed particles reach CCN-relevant sizes. The mean estimated CCN concentration during the autumn observation period was more than twice that during the spring observation period, suggesting that frequent NPF together with favorable particle-growth conditions may have contributed to higher CCN-relevant particle concentrations during the autumn measurements. These findings improve our understanding of the potential contribution of urban NPF to CCN-relevant particle populations in high-altitude environments over the Tibetan Plateau.

Despite the insights gained in this study, several limitations should be acknowledged. First, the day classification was based primarily on the daily PNSD evolution and modal development, supported by particle number concentrations in the 3–25 and 25–100 nm ranges and particle growth rates. Although these supporting metrics reduced reliance on visual inspection alone, some classification uncertainty remained for days with weak, discontinuous, or ambiguous particle evolution; these days were therefore retained as Undefined days and included in the non-NPF group for comparisons between NPF and non-NPF conditions. Second, CCN concentrations were not directly measured but estimated from the measured PNSD using the κ–Köhler framework, which may introduce uncertainties associated with the assumed hygroscopicity parameter and supersaturation. Therefore, the estimated CCN values are more suitable for interpreting relative differences and response patterns than for over-interpreting their absolute magnitudes. In addition, due to the lack of direct observations of VOCs and their oxidation products, the mechanisms of NPF, especially during the spring observation period, could not be further constrained. Future studies should combine longer-term continuous observations with direct CCN measurements and additional observations of VOCs, H_2SO_4, and related oxidation products, in order to better identify the controlling factors of NPF and its contribution to CCN in high-altitude urban environments over the Tibetan Plateau.

Code and data availability. The elevation data used in this study are openly available from the Geospatial Data Cloud at https://www.gscloud.cn (last access: 11 August 2026)).

The raw observational datasets used in this study have been deposited in Zenodo and can be freely downloaded from https://doi.org/10.5281/zenodo.19876491 (Zhao, 2026a).

The codes used for data processing and figure generation have been deposited in a separate Zenodo repository and can be freely downloaded from https://doi.org/10.5281/zenodo.19879178 (Zhao, 2026b).

Supplement. The supplement related to this article is available online at https://doi.org/10.5194/acp-26-11473-2026-supplement.

Author contributions. QM and LW wrote the manuscript. QM, LW, GZ, CY, JS and TZ discussed the original idea and results. JS, FS, TL, YG, and YC conducted the field measurement. QM, LW and JS processed and analysed the data.

Competing interests. The contact author has declared that none of the authors has any competing interests.

Disclaimer. Publisher's note: Copernicus Publications remains neutral with regard to jurisdictional claims made in the text, published maps, institutional affiliations, or any other geographical representation in this paper. The authors bear the ultimate responsibility for providing appropriate place names. Views expressed in the text are those of the authors and do not necessarily reflect the views of the publisher.

Financial support. This study was financially supported by the National Natural Science Foundation of China (grant not. 42405083), the Open Project of the Key Laboratory of Biodiversity and Environment on the Qinghai-Tibet Plateau, Ministry of Education (grant no. KLBE2025010), the Tibetan Key Research and Development Program Project (grant no. XZ202403ZY0022).

Review statement. This paper was edited by Imre Salma and reviewed by two anonymous referees.

References

Aktypis, A., Kaltsonoudis, C., Skyllakou, K., Matrali, A., Vasilakopoulou, C. N., Florou, K., and Pandis, S. N.: Infrequent new particle formation in a coastal Mediterranean city during the summer, Atmos. Environ., 302, 119732, https://doi.org/10.1016/j.atmosenv.2023.119732, 2023.

Arias, P., Bellouin, N., Coppola, E., Jones, R., Krinner, G., Marotzke, J., Naik, V., Palmer, M., Plattner, G.-K., and Rogelj, J.: Climate Change 2021: the physical science basis, in: Contribution of Working Group I to the Sixth Assessment Report of the Intergovernmental Panel on Climate Change; technical summary, Cambridge University Press, Cambridge, UK and New York, NY, USA, 33–144, https://doi.org/10.1017/9781009157896.002, 2021.

Baalbaki, R., Pikridas, M., Jokinen, T., Laurila, T., Dada, L., Bezantakos, S., Ahonen, L., Neitola, K., Maisser, A., Bimenyimana, E., Christodoulou, A., Unga, F., Savvides, C., Lehtipalo, K., Kangasluoma, J., Biskos, G., Petäjä, T., Kerminen, V. M., Sciare, J., and Kulmala, M.: Towards understanding the characteristics of new particle formation in the Eastern Mediterranean, Atmos. Chem. Phys., 21, 9223–9251, https://doi.org/10.5194/acp-21-9223-2021, 2021.

Bianchi, F., Junninen, H., Bigi, A., Sinclair, V. A., Dada, L., Hoyle, C. R., Zha, Q., Yao, L., Ahonen, L. R., Bonasoni, P., Buenrostro Mazon, S., Hutterli, M., Laj, P., Lehtipalo, K., Kangasluoma, J., Kerminen, V. M., Kontkanen, J., Marinoni, A., Mirme, S., Molteni, U., Petäjä, T., Riva, M., Rose, C., Sellegri, K., Yan, C., Worsnop, D. R., Kulmala, M., Baltensperger, U., and Dommen, J.: Biogenic particles formed in the Himalaya as an important source of free tropospheric aerosols, Nat. Geosci., 14, 4–9, https://doi.org/10.1038/s41561-020-00661-5, 2021.

Cai, R., Yang, D., Fu, Y., Wang, X., Li, X., Ma, Y., Hao, J., Zheng, J., and Jiang, J.: Aerosol surface area concentration: a governing factor in new particle formation in Beijing, Atmos. Chem. Phys., 17, 12327–12340, https://doi.org/10.5194/acp-17-12327-2017, 2017.

Casans, A., Casquero-Vera, J. A., Rejano, F., Lyamani, H., Cazorla, A., Zabala, I., Huang, W., Agro, M., Barreto, A., Rodriguez, S., Gonzalez, Y., Bianchi, F., Petaja, T., Olmo, F. J., Alados-Arboledas, L., Carinanos, P., Gysel-Beer, M., and Titos, G.: Determining the impact of new particle formation events on cloud condensation nuclei (CCN) concentrations, Sci. Total Environ., 972, 179094, https://doi.org/10.1016/j.scitotenv.2025.179094, 2025.

Cramer, K. L., Guenther, A. B., and Smith, J. N.: Ultrafine aerosol formation and growth in a Southern California desert, Aerosol Sci. Tech., 60, 665–677, https://doi.org/10.1080/02786826.2026.2619538, 2026.

Dal Maso, M., Kulmala, M., Riipinen, I., Wagner, R., Hussein, T.,Aalto, P. P., and Lehtinen, K. E.: Formation and growth of fresh atmospheric aerosols: eight years of aerosol size distribution data from SMEAR II, Hyytiälä, Finland, Boreal Environ. Res., 10, 323–336, 2005.

Dinoi, A., Weinhold, K., Wiedensohler, A., and Contini, D.: Study of new particle formation events in southern Italy, Atmos. Environ., 244, 117920, https://doi.org/10.1016/j.atmosenv.2020.117920, 2021.

Du, W., Zhao, J., Wang, Y., Zhang, Y., Wang, Q., Xu, W., Chen, C., Han, T., Zhang, F., Li, Z., Fu, P., Li, J., Wang, Z., and Sun, Y.: Simultaneous measurements of particle number size distributions at ground level and 260 m on a meteorological tower in urban Beijing, China, Atmos. Chem. Phys., 17, 6797–6811, https://doi.org/10.5194/acp-17-6797-2017, 2017.

Gao, Z., Wang, F., Du, W., Wang, S., Sun, Y., Yang, W., Wang, X., Han, B., and Bai, Z.: Elucidating particle number concentrations and unveiling source mechanisms at a prominent national background site on the northeastern Qinghai-Tibetan Plateau, Sci. Total Environ., 969, 178928, https://doi.org/10.1016/j.scitotenv.2025.178928, 2025.

Hakala, S., Vakkari, V., Bianchi, F., Dada, L., Deng, C., Dällenbach, K., Fu, Y., Jiang, J., Kangasluoma, J., and Kujansuu, J.: Observed coupling between air mass history, secondary growth of nucleation mode particles and aerosol pollution levels in Beijing, Environ. Sci.: Atmos., 2, 146–164, 2022.

Hong, J., Tang, M., Wang, Q., Ma, N., Zhu, S., Zhang, S., Pan, X., Xie, L., Li, G., Kuhn, U., Yan, C., Tao, J., Kuang, Y., He, Y., Xu, W., Cai, R., Zhou, Y., Wang, Z., Zhou, G., Yuan, B., Cheng, Y., and Su, H.: Measurement Report: Wintertime new particle formation in the rural area of the North China Plain – influencing factors and possible formation mechanism, Atmos. Chem. Phys., 23, 5699–5713, https://doi.org/10.5194/acp-23-5699-2023, 2023.

Hu, Y., Yu, H., Kang, S., Yang, J., Rai, M., Yin, X., Chen, X., and Chen, P.: Aerosol–meteorology feedback diminishes the transboundary transport of black carbon into the Tibetan Plateau, At-

mos. Chem. Phys., 24, 85–107, https://doi.org/10.5194/acp-24-85-2024, 2024.

Hussein, T., Atashi, N., Sogacheva, L., Hakala, S., Dada, L., Petäjä, T., and Kulmala, M.: Characterization of Urban New Particle Formation in Amman – Jordan, Atmosphere, 11, 79, https://doi.org/10.3390/atmos11010079, 2020.

Kalivitis, N., Kerminen, V. M., Kouvarakis, G., Stavroulas, I., Tzitzikalaki, E., Kalkavouras, P., Daskalakis, N., Myriokefalitakis, S., Bougiatioti, A., Manninen, H. E., Roldin, P., Petäjä, T., Boy, M., Kulmala, M., Kanakidou, M., and Mihalopoulos, N.: Formation and growth of atmospheric nanoparticles in the eastern Mediterranean: results from long-term measurements and process simulations, Atmos. Chem. Phys., 19, 2671–2686, https://doi.org/10.5194/acp-19-2671-2019, 2019.

Kalkavouras, P., Bougiatioti, A., Kalivitis, N., Stavroulas, I., Tombrou, M., Nenes, A., and Mihalopoulos, N.: Regional new particle formation as modulators of cloud condensation nuclei and cloud droplet number in the eastern Mediterranean, Atmos. Chem. Phys., 19, 6185–6203, https://doi.org/10.5194/acp-19-6185-2019, 2019.

Kalkavouras, P., Bougiatioti, A., Grivas, G., Stavroulas, I., Kalivitis, N., Liakakou, E., Gerasopoulos, E., Pilinis, C., and Mihalopoulos, N.: On the regional aspects of new particle formation in the Eastern Mediterranean: A comparative study between a background and an urban site based on long term observations, Atmos. Res., 239, 104911, https://doi.org/10.1016/j.atmosres.2020.104911, 2020.

Kalkavouras, P., BougiatiotI, A., Hussein, T., Kalivitis, N., Stavroulas, I., Michalopoulos, P., and Mihalopoulos, N.: Regional New Particle Formation over the Eastern Mediterranean and Middle East, Atmosphere, 12, 13, https://doi.org/10.3390/atmos12010013, 2021.

Kerminen, V.-M., Chen, X., Vakkari, V., Petäjä, T., Kulmala, M., and Bianchi, F.: Atmospheric new particle formation and growth: review of field observations, Environ. Res. Lett., 13, 103003, https://doi.org/10.1088/1748-9326/aadf3c, 2018.

Kulmala, M., Maso, M. D., Mäkelä, J., Pirjola, L., Väkevä, M., Aalto, P., Miikkulainen, P., Hämeri, K., and O'dowd, C.: On the formation, growth and composition of nucleation mode particles, Tellus B, 53, 479–490, 2001.

Kulmala, M., Petäjä, T., Nieminen, T., Sipilä, M., Manninen, H. E., Lehtipalo, K., Dal Maso, M., Aalto, P. P., Junninen, H., Paasonen, P., Riipinen, I., Lehtinen, K. E. J., Laaksonen, A., and Kerminen, V.-M.: Measurement of the nucleation of atmospheric aerosol particles, Nat. Protoc., 7, 1651–1667, 10.1038/nprot.2012.091, 2012.

Lai, S., Qi, X., Huang, X., Lou, S., Chi, X., Chen, L., Liu, C., Liu, Y., Yan, C., Li, M., Liu, T., Nie, W., Kerminen, V. M., Petäjä, T., Kulmala, M., and Ding, A.: New particle formation induced by anthropogenic–biogenic interactions on the southeastern Tibetan Plateau, Atmos. Chem. Phys., 24, 2535–2553, https://doi.org/10.5194/acp-24-2535-2024, 2024.

Lampilahti, A., Garmash, O., Aliaga, D., Arshinov, M., Davydov, D., Belan, B., Lampilahti, J., Kerminen, V.-M., Petäjä, T., Kulmala, M., and Ezhova, E.: Insights into new particle formation in a Siberian boreal forest from nanoparticle ranking analysis, Aerosol Res., 3, 441–459, https://doi.org/10.5194/ar-3-441-2025, 2025.

Li, K., An, Y., Xu, J., Zhong, M., Zhao, W., and Qin, X.: Measurement report: Year-long chemical composition, optical properties, and sources of atmospheric aerosols in the northeastern Tibetan Plateau, Atmos. Chem. Phys., 25, 12433–12450, https://doi.org/10.5194/acp-25-12433-2025, 2025.

Liu, Y., Nie, W., Qi, X., Li, Y., Xu, T., Liu, C., Ge, D., Chen, L., Niu, G., Wang, J., Yang, L., Wang, L., Zhu, C., Wang, J., Zhang, Y., Liu, T., Zha, Q., Yan, C., Ye, C., Zhang, G., Hu, R., Huang, R.-J., Chi, X., Zhu, T., and Ding, A.: The Pivotal Role of Heavy Terpenes and Anthropogenic Interactions in New Particle Formation on the Southeastern Qinghai-Tibet Plateau, Environ. Sci. Technol., 58, 19748–19761, https://doi.org/10.1021/acs.est.4c04112, 2024.

Olin, M., Kuuluvainen, H., Aurela, M., Kalliokoski, J., Kuittinen, N., Isotalo, M., Timonen, H. J., Niemi, J. V., Rönkkö, T., and Dal Maso, M.: Traffic-originated nanocluster emission exceeds H_2SO_4-driven photochemical new particle formation in an urban area, Atmos. Chem. Phys., 20, 1–13, https://doi.org/10.5194/acp-20-1-2020, 2020.

Petters, M. D. and Kreidenweis, S. M.: A single parameter representation of hygroscopic growth and cloud condensation nucleus activity, Atmos. Chem. Phys., 7, 1961–1971, https://doi.org/10.5194/acp-7-1961-2007, 2007.

Rose, C., Sellegri, K., Moreno, I., Velarde, F., Ramonet, M., Weinhold, K., Krejci, R., Andrade, M., Wiedensohler, A., Ginot, P., and Laj, P.: CCN production by new particle formation in the free troposphere, Atmos. Chem. Phys., 17, 1529–1541, https://doi.org/10.5194/acp-17-1529-2017, 2017.

Saha, P. K., Robinson, E. S., Shah, R. U., Zimmerman, N., Apte, J. S., Robinson, A. L., and Presto, A. A.: Reduced Ultrafine Particle Concentration in Urban Air: Changes in Nucleation and Anthropogenic Emissions, Environ. Sci. Technol., 52, 6798–6806, https://doi.org/10.1021/acs.est.8b00910, 2018.

Sellegri, K., Rose, C., Marinoni, A., Lupi, A., Wiedensohler, A., Andrade, M., Bonasoni, P., and Laj, P.: New Particle Formation: A Review of Ground-Based Observations at Mountain Research Stations, Atmosphere, 10, 493, https://doi.org/10.3390/atmos10090493, 2019.

Shang, D., Hu, M., Zheng, J., Qin, Y., Du, Z., Li, M., Fang, J., Peng, J., Wu, Y., Lu, S., and Guo, S.: Particle number size distribution and new particle formation under the influence of biomass burning at a high altitude background site at Mt. Yulong (3410 m), China, Atmos. Chem. Phys., 18, 15687–15703, https://doi.org/10.5194/acp-18-15687-2018, 2018.

Shang, D., Tang, L., Fang, X., Wang, L., Yang, S., Wu, Z., Chen, S., Li, X., Zeng, L., Guo, S., and Hu, M.: Variations in source contributions of particle number concentration under long-term emission control in winter of urban Beijing, Environ. Pollut., 304, 119072, https://doi.org/10.1016/j.envpol.2022.119072, 2022.

Shen, L., Wang, H., Yin, Y., Chen, J., and Chen, K.: Observation of atmospheric new particle growth events at the summit of mountain Tai (1534 m) in Central East China, Atmos. Environ., 201, 148–157, 2019.

Shen, X., Sun, J., Ma, Q., Zhang, Y., Zhong, J., Yue, Y., Xia, C., Hu, X., Zhang, S., and Zhang, X.: Long-term trend of new particle formation events in the Yangtze River Delta, China and its influencing factors: 7-year dataset analysis, Sci. Total Environ., 807, 150783, https://doi.org/10.1016/j.scitotenv.2021.150783, 2022.

Singh, K., Gautam, A. S., Jeni Victor, N., Kumar, S., Potdar, S. S., Komsaare, K., and Siingh, D.: Characteristics of new particle formation events at high-altitude location of Western Himalayan Region, Tehri Garhwal, India, Atmos. Res., 315, 107903, https://doi.org/10.1016/j.atmosres.2024.107903, 2025.

Tang, L., Hu, M., Shang, D., Fang, X., Mao, J., Xu, W., Zhou, J., Zhao, W., Wang, Y., Zhang, C., Zhang, Y., Hu, J., Zeng, L., Ye, C., Guo, S., and Wu, Z.: High frequency of new particle formation events driven by summer monsoon in the central Tibetan Plateau, China, Atmos. Chem. Phys., 23, 4343–4359, https://doi.org/10.5194/acp-23-4343-2023, 2023.

Venzac, H., Sellegri, K., Laj, P., Villani, P., Bonasoni, P., Marinoni, A., Cristofanelli, P., Calzolari, F., Fuzzi, S., Decesari, S., Facchini, M.-C., Vuillermoz, E., and Verza, G. P.: High frequency new particle formation in the Himalayas, P. Natl. Acad. Sci. USA, 105, 15666–15671, https://doi.org/10.1073/pnas.0801355105, 2008.

Victor, J. N., Buchunde, P., Sebastian, M., Kanawade, V. P., Siingh, D., Mukherjee, S., Potdar, S. S., Dharmaraj, T., and Pandithurai, G.: Characteristics of new particle formation events in a mountain semi-rural location in India, Atmos. Environ., 324, 120414, https://doi.org/10.1016/j.atmosenv.2024.120414, 2024.

Wang, J., Li, M., Li, L., Zheng, R., Fan, X., Hong, Y., Xu, L., Chen, J., and Hu, B.: Particle number size distribution and new particle formation in Xiamen, the coastal city of Southeast China in wintertime, Sci. Total Environ., 826, 154208, https://doi.org/10.1016/j.scitotenv.2022.154208, 2022.

Wu, H., Li, Z., Jiang, M., Liang, C., Zhang, D., Wu, T., Wang, Y., and Cribb, M.: Contributions of traffic emissions and new particle formation to the ultrafine particle size distribution in the megacity of Beijing, Atmos. Environ., 262, 118652, https://doi.org/10.1016/j.atmosenv.2021.118652, 2021.

Wu, H., Li, Z., Hai, S., Gao, Y., Jiang, J., Zhao, B., Cribb, M., Zhang, D., Pu, D., Liu, M., Wang, C., Lan, J., and Wang, Y.: Vertical transport of ultrafine particles and turbulence evolution impact on new particle formation at the surface & Canton Tower, Atmos. Res., 302, https://doi.org/10.1016/j.atmosres.2024.107290, 2024.

Yang, C., Brean, J., Xu, W., Xu, L., Huang, W., Fan, X., Bianchi, F., Du, W., Lin, Z., Li, L., Chen, G., Zhang, Y., Cai, R., Chen, Y., Li, M., and Chen, J.: Anthropogenic Oxygenated Organic Molecules Dominate New Particle Growth in Moderate-Pollution Urban China, Environ. Sci. Technol., 60, 6364–6377, https://doi.org/10.1021/acs.est.5c11555, 2026.

Yao, L., Garmash, O., Bianchi, F., Zheng, J., Yan, C., Kontkanen, J., Junninen, H., Mazon, S. B., Ehn, M., and Paasonen, P.: Atmospheric new particle formation from sulfuric acid and amines in a Chinese megacity, Science, 361, 278–281, 2018.

Yeganeh, B., Shakerdonyavi, A., Zafarmomen, N., and Taheri, A.: Comprehensive spatiotemporal analysis of long-term mobile monitoring for traffic-related particles in a complex urban environment, Atmos. Pollut. Res., 17, 102870, https://doi.org/10.1016/j.apr.2025.102870, 2026.

Zhang, K., Xu, Z., Zhang, F., and Wang, Z.: Unveiling the organic contribution to the initial particle growth in 3–10 nm size range, Atmos. Chem. Phys., 26, 2241–2254, https://doi.org/10.5194/acp-26-2241-2026, 2026.

Zhang, Q., Jia, S., Yang, L., Krishnan, P., Zhou, S., Shao, M., and Wang, X.: New particle formation (NPF) events in China urban clusters given by sever composite pollution background, Chemosphere, 262, 127842, https://doi.org/10.1016/j.chemosphere.2020.127842, 2021.

Zhao, G.: High Frequency of Urban New Particle Formation on the Tibetan Plateau: Quantifying Formation Rates, Growth Rates, and CCN Production [Dataset], Zenodo [data set], https://doi.org/10.5281/zenodo.19876491, 2026a.

Zhao, G.: High Frequency of Urban New Particle Formation on the Tibetan Plateau: Quantifying Formation Rates, Growth Rates, and CCN Production Codes [Dataset], Zenodo [code], https://doi.org/10.5281/zenodo.19879178, 2026b.

Zhao, W., Zhang, X., Zhai, L., Shen, X., and Xu, J.: Chemical characterization and sources of submicron aerosols in Lhasa on the Qinghai–Tibet Plateau: Insights from high-resolution mass spectrometry, Sci. Total Environ., 815, 152866, https://doi.org/10.1016/j.scitotenv.2021.152866, 2022.